Effects of fracture intersections on seismic dispersion: theoretical predictions versus numerical simulations

Junxin Guo[1]*, J. Germán Rubino[2,4], Stanislav Glubokovskikh[1] and Boris Gurevich[1,3]

[1]*Department of Exploration Geophysics, Curtin University, GPO Box U1987, Perth, WA 6845, Australia*, [2]*Department of Earth Sciences, Western University, London, ON N6A 5B7, Canada*, [3]*CSIRO Energy Flagship, 26 Dick Perry Avenue, Kensington, WA 6152, Australia, and* [4]*CONICET, Centro Atómico Bariloche - CNEA, San Carlos de Bariloche, Argentina*

ABSTRACT

The detection and characterisation of domains of intersecting fractures are important goals in several disciplines of current interest, including exploration and production of unconventional reservoirs, nuclear waste storage, CO_2 sequestration, and groundwater hydrology, among others. The objective of this study is to propose a theoretical framework for quantifying the effects of fracture intersections on the frequency-dependent elastic properties of fluid-saturated porous and fractured rocks. Three characteristic frequency regimes for fluid pressure communication are identified. In the low-frequency limit, fractures are in full pressure communication with the embedding porous matrix and with other fractures. Conversely, in the high-frequency limit, fractures are hydraulically isolated from the matrix and from other fractures. At intermediate frequencies, fractures are hydraulically isolated from the matrix porosity but can be in hydraulic communication with each other, depending on whether fracture sets are intersecting. For each frequency regime, the effective stiffness coefficients are derived using the linear-slip theory and anisotropic Gassmann equations. Explicit mathematical expressions for the two characteristic frequencies that separate the three frequency regimes are also determined. Theoretical predictions are then applied to two synthetic 2D samples, each containing two orthogonal fracture sets: one with and another without intersections. The resulting stiffness coefficients, Thomsen-style anisotropy parameters, and the transition frequencies show good agreement with corresponding numerical simulations. The theoretical results are applicable not only to 2D but also to 3D fracture systems and are amenable to being employed in inversion schemes designed to characterise fracture systems.

Key words: Rock physics, Fractures, Theory, Numerical study.

1 INTRODUCTION

One of the challenges in unconventional oil and gas exploration is finding the so-called sweet spots. Sweet spots are areas of elevated fracture permeability, which often result from the presence of multiple intersecting sets of open natural fractures. Thus, detecting and characterising domains of intersecting fractures are important for the proper management of unconventional reservoirs. Furthermore, this kind of information is also crucial for the monitoring of CO_2 sequestration and nuclear waste storage, as these operations may fail due to leakage of fluids through connected fracture networks (Neuzil 2013; Luo and Bryant 2014). Apart from these, there are many other areas where the importance of detecting such fractured domains can be found, such as tunnel engineering, groundwater and contaminant hydrology, and mining

---

*E-mail: junxin.guo@postgrad.curtin.edu.au

engineering (e.g., Grenon and Hadjigeorgiou 2012; Lisjak, Figi, and Grasselli 2014; Karay and Hajnal 2015). The seismic method is currently considered as a potentially important tool for detecting and characterising fractured rocks, as seismic waves travelling through this kind of media experience anisotropy, attenuation, and dispersion (Rubino *et al.* 2013, 2014, 2015).

Distinguishing intersecting from non-intersecting fractures using seismic data is challenging, since intersections of fractures have little effect on static elastic properties (Grechka and Kachanov 2006). However, for fluid-saturated rocks at finite frequencies, intersecting fracture sets may exhibit somewhat different properties. Indeed, when a seismic wave compresses a fluid-filled fracture, it induces a fluid pressure increment within that fracture. This increment will be lower if the fracture is in pressure communication with another fracture of a different orientation, resulting in an increase in fracture compliance. This effect of fluid pressure communication within fractures having different orientations depends on the frequency and hydraulic conductivity of the fracture system. For isotropic or transversely isotropic distributions of fractures, this effect has been explored in a number of publications (O'Connell and Budiansky 1977; Jones 1986; Endres and Knight 1997; Chapman, Zatsepin, and Crampin 2002; Guéguen and Sarout 2009; Sarout 2012). Other authors explored the effect of pressure communication between fractures and background porosity, but these studies are often limited to a single set of parallel fractures or random distributions of fracture orientations (see, e.g., Chapman (2003), Gurevich (2003), Jakobsen (2004), and Gurevich *et al.* (2009)).

Rubino *et al.* (2013, 2014, 2015) have explored this effect by determining the frequency-dependent elastic properties of porous rocks permeated by two orthogonal sets of open fractures using a numerical algorithm based on the theory of poroelasticity. In particular, Rubino *et al.* (2015) performed simulations for both intersecting and non-intersecting fracture sets and showed significant differences between the observed elastic properties. These results are very promising for seismic characterisation of unconventional reservoirs; however, performing numerical simulations for every configuration of fractures is impractical, especially for inverse problems. Hence, it is important to predict these effects theoretically. The aim of this paper is to find theoretical expressions that can quantify the effects of fracture intersections on the frequency-dependent elastic properties of rocks and compare these theoretical predictions with the numerical simulations of Rubino *et al.* (2013, 2014, 2015).

2 NUMERICAL SIMULATIONS

2.1 Upscaling procedure

Following the work of Rubino *et al.* (2015), we model 2D fractured rocks in the framework of Biot's theory of poroelasticity (Biot 1941), with the fractures represented as highly compliant and permeable heterogeneities embedded in a stiffer porous background. Both the fractures and the background are fluid saturated, and fluid pressure communication between the fractures and the background and between connected fractures can take place.

To estimate the effective seismic properties of fractured reservoirs, we employ a numerical upscaling procedure based on the application of three oscillatory relaxation tests on a square sample representative of the medium of interest (Rubino *et al.* 2016). First, we apply homogeneous time-harmonic normal displacements on the top and bottom boundaries of the sample, whereas the lateral boundaries are confined. As we are interested in the undrained response, we do not allow the fluid to flow into or out of the sample. Next, a second test similar to the previous one is applied, but the normal displacements are applied on the lateral boundaries of the sample. Finally, in a third test, we apply a simple shear to the probed sample.

To account for fluid-pressure diffusion effects on the seismic properties of the considered fractured media, the solid and relative fluid displacements in response to the three tests are obtained by solving, through a finite-element approach and under corresponding boundary conditions, Biot's quasi-static poroelastic equations (Biot 1941) in the space–frequency domain:

$$\nabla \cdot \sigma = 0, \tag{1}$$

$$i\omega \frac{\eta}{\kappa} w = -\nabla p_f, \tag{2}$$

where σ is the total stress tensor, ω is the angular frequency, p_f is the fluid pressure, w is the average relative fluid displacement, κ is the rock permeability, and η is the shear viscosity of the pore fluid.

Next, for each test, we compute the volume averages of the stress and strain components:

$$\langle \varepsilon_{ij}^k \rangle = \frac{1}{V} \int_\Omega \varepsilon_{ij}^k dV, \tag{3}$$

$$\langle \sigma_{ij}^k \rangle = \frac{1}{V} \int_\Omega \sigma_{ij}^k dV, \tag{4}$$

where ε is the strain tensor, Ω is the domain of volume V that represents the probed sample, and $k = 1,2,3$ denotes the kth oscillatory test previously described.

Assuming that the average responses of the probed sample can be represented by an equivalent homogeneous anisotropic viscoelastic solid, the average strain and stress components can be connected through a complex-valued frequency-dependent equivalent Voigt stiffness matrix $\mathbf{C}^{2D}$:

$$\begin{pmatrix} \langle \sigma_{11}^k \rangle \\ \langle \sigma_{22}^k \rangle \\ \langle \sigma_{12}^k \rangle \end{pmatrix} = \begin{pmatrix} C_{11} & C_{12} & C_{16} \\ C_{12} & C_{22} & C_{26} \\ C_{16} & C_{26} & C_{66} \end{pmatrix} \begin{pmatrix} \langle \varepsilon_{11}^k \rangle \\ \langle \varepsilon_{22}^k \rangle \\ \langle 2\varepsilon_{12}^k \rangle \end{pmatrix}. \tag{5}$$

It should be noted that the stiffness coefficients in equation (5) are similar to those of the corresponding 3D samples under the plane strain condition.

Equation (5) holds for the three oscillatory tests previously described. Therefore, we establish nine equations, and the six unknown stiffness coefficients are computed using a classic least squares algorithm. Readers are referred to the work of Rubino *et al.* (2016) for the details of the numerical upscaling procedure.

It is important to notice here that a slightly different numerical approach has been proposed by Vinci, Renner, and Steeb (2014), who model flow within fractures using Navier–Stokes equations. However, the methodology of Vinci *et al.* (2014) does not consider generic anisotropy of the probed synthetic sample, and the results have only been reported for a set of two intersecting fractures. This implies that their results are unsuitable for comparison with an equivalent-medium theory.

2.2 Results

Two synthetic 2D fractured rock samples considered by Rubino *et al.* (2015) are shown in Fig. 1. Both samples have dimensions of 20 cm × 20 cm and contain 20 horizontal and 20 vertical fractures. The main difference between the samples, therefore, is that, in sample (a), fractures do not intersect, whereas in sample (b), most fractures show some degree of connectivity. This ensures that the differences between their frequency-dependent elastic properties are predominantly caused by the fracture intersections. The coordinate system is established (Fig. 1) such that the vertical fractures are perpendicular to the x-axis and the horizontal fractures are perpendicular to the y-axis. The samples are long enough along the z-axis to make sure that the normal and shear strains along the z-axis are negligible, thus satisfying

the condition of plane strain. This reduces the 3D problem to a 2D problem.

Both the fractures and the background are assumed to be fully saturated with water, with bulk modulus $K_f = 2.25$ GPa, density $\rho_f = 1.09$ g/cm^3, and viscosity $\eta_f = 0.001$ Pa s. We assume that the background is characterised by grain bulk modulus $K_g = 37$ GPa and density $\rho_g = 2.65$ g/cm^3. The remaining physical properties of the background are as follows (Rubino *et al.* 2015): dry frame bulk modulus $K_b = 26$ GPa, shear modulus $G_b = 31$ GPa, porosity $\phi_b = 0.1$, and permeability $\kappa_b = 0.0001$ mD.

The fractures are inclusions of rectangular geometry, with lengths of ~4 cm and apertures of 0.06 cm containing a porous material, with the bulk and shear moduli of the dry fractures K_{fr} and G_{fr} being of values 0.04 and 0.02 GPa, respectively, which is consistent with a fracture shear compliance value of 3×10^{-11} m/Pa and a drained normal compliance value of 10^{-11} m/Pa, as employed by Nakagawa and Schoenberg (2007). The grain moduli of this fracture infill material are assumed to be the same as those in the background. This porous fracture infill material is characterised by a porosity ϕ_{fr} of 0.8 and permeability κ_{fr} of 100 D. It should be noticed here that such permeability value is significantly lower than that corresponding to the cubic law for the considered fracture aperture (Witherspoon *et al.* 1980). However, this is consistent with the fact that, while the cubic law is valid only for flow between two parallel plates, natural fractures tend to be "rough walled", with the walls being in contact with each other at certain locations. Moreover, the regions between the contact areas often contain rock fragments, weathering products, or mineral deposits, which tend to significantly reduce the effective permeability of the fracture.

Using the numerical approach and the physical parameters previously described, the equivalent stiffness coefficients for the two samples are obtained for frequencies varying from 10^{-5} to 10^8 Hz. It is important to mention that such a wide frequency range may violate the quasi-static condition, as the higher frequencies may be larger than Biot's characteristic frequency (Biot 1962; Dutta and Odé 1979). In addition, effective seismic properties can be determined provided that the heterogeneities are much smaller than the considered seismic wavelengths, which is not satisfied for the higher frequencies analysed in the simulations. However, considering such a wide frequency range is very useful in analysing the physics in terms of the transition from relaxed to unrelaxed states, which is a common practice in works dealing with effective media. In addition, the frequency ranges where dispersion takes place
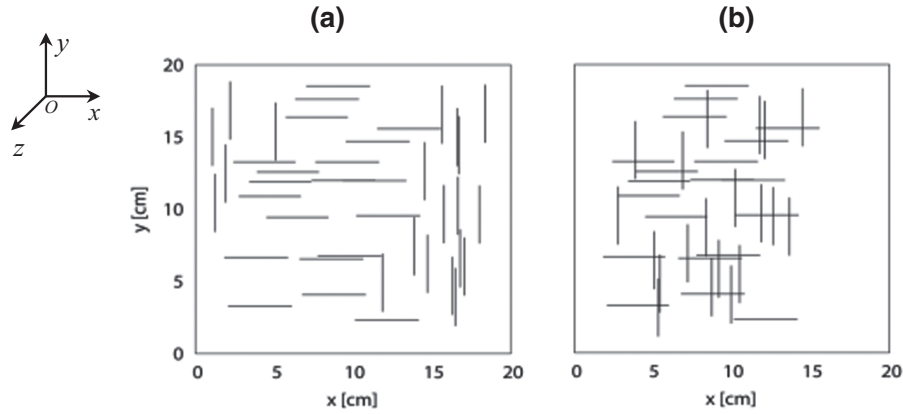
Figure 1 Two-dimensional rock samples containing (a) non-intersecting fracture sets and (b) intersecting fracture sets.

are mainly controlled by the permeabilities of the involved materials. This implies that, for materials with lower permeabilities, the features taking place above the aforementioned threshold frequencies would shift towards lower frequencies, eventually below such threshold values, thus showing that the results obtained here for unrealistically high frequencies may be useful in other situations.

The obtained numerical results show that, for most of the considered frequencies, the values of C_{16} and C_{26} are below 0.5 GPa, and their maximum values do not exceed 1 GPa. These values are negligibly small compared with the remaining stiffness coefficients C_{11}, C_{12}, C_{22}, and C_{66}, and hence, only these four coefficients are considered in the analysis, as shown in Fig. 2 (solid lines). To illustrate the influence of the fluid, we also compute the stiffness coefficients for the dry samples by choosing the fluid bulk modulus to be negligibly small. The results are shown as open triangles in Fig. 2. Significant effects of fluid saturation on the stiffness coefficients can be observed. Comparing the samples with and without intersecting fractures, it is found that the values of the stiffness coefficients at the low- and high-frequency limits are close. However, for the sample with intersecting fractures, one can observe a plateau at intermediate frequencies. The stiffness coefficients in this frequency range are quite different from those for the sample with non-intersecting fractures. Therefore, fracture intersections have great influence on the frequency-dependent elastic properties of the samples.

3 THEORY

To quantify the influence of fracture intersections, we propose a theoretical framework that provides the elastic properties of saturated fractured rocks for the two frequency limits and the

intermediate frequency range, as well as the characteristic frequencies that separate these three regimes. Here, we derive the formulas for the general 3D case. The resulting stiffness coefficients in the *x–y* plane (C_{11}, C_{12}, C_{22}, and C_{66}) can be directly compared with the results of 2D numerical simulations under plane strain conditions.

3.1 Dry fracture compliance

It is convenient to characterise dry fractured rocks using the linear-slip theory, in which the compliance matrix of the fractured rock $\mathbf{S}^0$ is expressed as a sum of the compliance matrix of the background rock $\mathbf{S}_b$ plus a number of matrices $\mathbf{S}_{ci}$ expressing the normal and tangential fracture compliance values, Z_N and Z_T, for each fracture set (e.g., Schoenberg and Sayers 1995):

$$\mathbf{S}^0 = \mathbf{S}_b + \sum_{i=1}^{m} \mathbf{S}_{ci}, \tag{6}$$

where *m* is the number of fracture sets. $\mathbf{S}_b$ takes the following form for an isotropic background:

$$\mathbf{S}_b = \begin{pmatrix} 1/E_b & -v_b/E_b & -v_b/E_b & 0 & 0 & 0 \\ -v_b/E_b & 1/E_b & -v_b/E_b & 0 & 0 & 0 \\ -v_b/E_b & -v_b/E_b & 1/E_b & 0 & 0 & 0 \\ 0 & 0 & 0 & \frac{2(1+v_b)}{E_b} & 0 & 0 \\ 0 & 0 & 0 & 0 & \frac{2(1+v_b)}{E_b} & 0 \\ 0 & 0 & 0 & 0 & 0 & \frac{2(1+v_b)}{E_b} \end{pmatrix}, \tag{7}$$

where E_b and v_b are Young's modulus and Poisson's ratio of the dry background medium, respectively. For the samples shown in Fig. 1, the compliance matrix for the fracture set
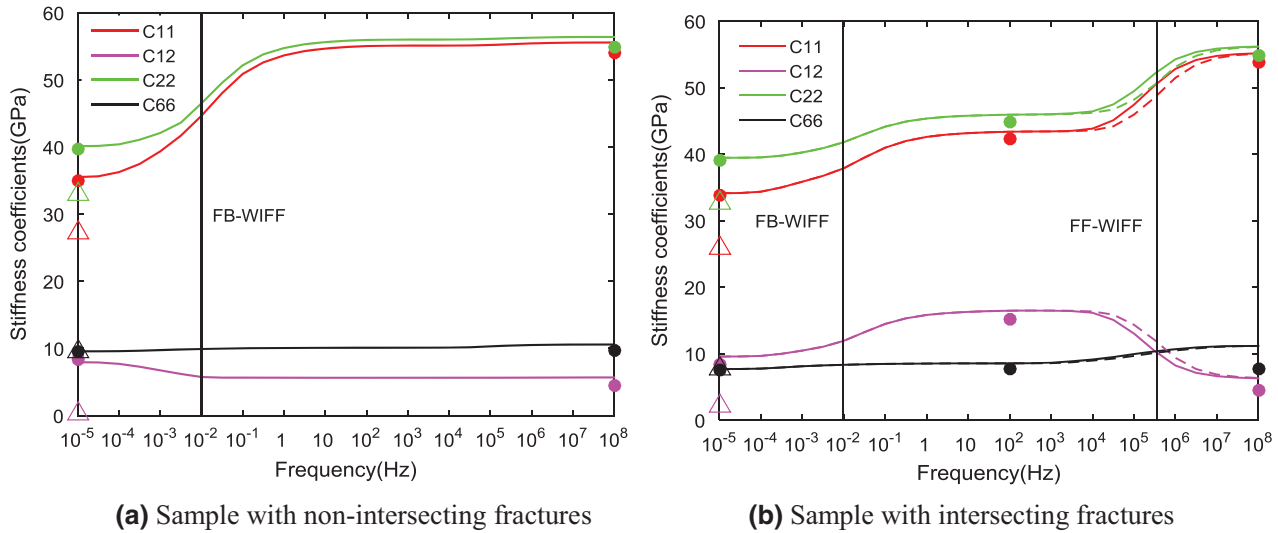
Figure 2 (Solid lines) Numerical simulations and (solid circles) theoretical predictions for the real part of the frequency-dependent stiffness coefficients. (Vertical solid lines) The two characteristic frequencies and (open triangles) the dry sample stiffness coefficients are also plotted. Fracture permeability is doubled to investigate its influence on the characteristic frequencies for (dashed lines) the sample with intersecting fractures.

perpendicular to x-direction $\mathbf{S}_{c1}$ and that for the other fracture set $\mathbf{S}_{c2}$ are as follows:

$$
\mathbf{S}_{c1} = \begin{pmatrix}
Z_{N1} & 0 & 0 & 0 & 0 & 0 \\
0 & 0 & 0 & 0 & 0 & 0 \\
0 & 0 & 0 & 0 & 0 & 0 \\
0 & 0 & 0 & 0 & 0 & 0 \\
0 & 0 & 0 & 0 & Z_{T3} & 0 \\
0 & 0 & 0 & 0 & 0 & Z_{T1}
\end{pmatrix},
\tag{8}
$$

$$
\mathbf{S}_{c2} = \begin{pmatrix}
0 & 0 & 0 & 0 & 0 & 0 \\
0 & Z_{N2} & 0 & 0 & 0 & 0 \\
0 & 0 & 0 & 0 & 0 & 0 \\
0 & 0 & 0 & Z_{T4} & 0 & 0 \\
0 & 0 & 0 & 0 & 0 & 0 \\
0 & 0 & 0 & 0 & 0 & Z_{T2}
\end{pmatrix}.
\tag{9}
$$

Here, the two tangential compliance values of each fracture set could be different if no rotational symmetry is found around the fracture normal due to the different fracture lengths in different directions (Far, Thomsen, and Sayers 2013), which is the case for our 2D samples under the plane strain condition. Thus, six dry fracture compliance values (Z_{N1}, Z_{T1}, Z_{T3}, Z_{N2}, Z_{T2}, and Z_{T4}) are essential in general 3D cases for the estimation of the elastic properties of the dry samples and, therefore, for those of the saturated samples at different frequencies. However, for the calculations of the elastic properties of the 2D samples investigated in this paper, only four fracture compliance values are needed: Z_{N1},

Z_{T1}, Z_{N2}, and Z_{T2}. To calculate their values, we apply the theoretical formulas for 2D crack compliance values using a non-interactive approximation (Kachanov and Sevostianov 2005) as follows:

$$
Z_{Ni} = \frac{n_i \pi L^2}{2 E_b^{2D} A}, i = 1, 2,
\tag{10}
$$

$$
Z_{Ti} = Z_{Ni}, i = 1, 2,
\tag{11}
$$

where n_i is the number of fractures of the corresponding fracture set, L is the length of the fracture, A is the surface area of the 2D sample, and E_b^{2D} is the 2D Young's modulus for the background medium, which has the following relation with 3D parameters:

$$
E_b^{2D} = \frac{E_b}{1 - \nu_b^2}.
\tag{12}
$$

Equations (10) and (11) can be used to compute the dry fracture compliance values. To assess their accuracy, we compute the dry stiffness coefficients of the samples using these fracture compliance values through equation (6) and compare them with those provided by the numerical simulations for dry fractured samples. For the sample with intersecting fractures, the results are shown in Table 1 (columns 2 and 3). We find that there are significant discrepancies between theoretical predictions and the numerical simulations, especially for C_{12} and C_{66} that show the largest relative differences. For further comparison, we can compute Thomsen-style anisotropy

Table 1 Comparison of the stiffness coefficients of the dry sample with intersecting fractures computed using numerical simulations and linear-slip theory with theoretical fracture compliance values

	Numerical simulations	Linear-slip theory with theoretical fracture compliance values
C_{11} (GPa)	25.82	29.69
C_{12} (GPa)	2.07	1.05
C_{22} (GPa)	32.57	29.69
C_{66} (GPa)	7.65	14.32

parameters for orthotropic media (Tsvankin 1997). For 2D geometry, the relevant anisotropy parameters are $\varepsilon^{(3)}$ and $\delta^{(3)}$ (Tsvankin 1997; Collet *et al.* 2014):

$$\varepsilon^{(3)} = \frac{C_{22} - C_{11}}{2C_{11}}, \tag{13}$$

$$\delta^{(3)} = \frac{(C_{12} + C_{66})^2 - (C_{11} - C_{66})^2}{2C_{11}(C_{11} - C_{66})}. \tag{14}$$

The theoretical predictions (Kachanov and Sevostianov 2005) indicate that both $\delta^{(3)}$ and $\varepsilon^{(3)}$ are equal to zero, i.e., the theory predicts the sample to be isotropic in the x–y plane. However, the numerical simulations give values of $\varepsilon^{(3)} = 0.13$ and $\delta^{(3)} = -0.25$, which are clearly not even close to zero. Thus, numerical simulations show that the dry fractured sample is actually anisotropic in the x–y plane, and this anisotropy is anelliptical. In the case of the sample with non-intersecting fractures, we observe similar disagreement between the prediction of the effective-medium theory and numerical results. These discrepancies suggest that it is not appropriate to use the theoretical non-interactive effective-medium approximation [equations (10) and (11)] in calculating the dry fracture compliance values of the 2D samples investigated in this paper.

A possible cause for the failure in the theoretical formulas of dry fracture compliance values may be boundary effects due to the limited volume of the samples. We notice that, in increasing the sample volume fourfold while keeping the other properties comparable with the original ones, the discrepancies between the theoretical approach and the numerical simulations become smaller. However, these discrepancies do not vanish. This implies that there may be additional reasons for these discrepancies, such as the finite aspect ratio of the fractures, relatively large crack densities, or the rectangular shape of the cracks, which are features ignored in the non-interactive

effective-medium approximation. A careful analysis on this will be carried out in the future.

Indeed, in a recent work, Yousef and Angus (2016) have found that the linear-slip theory may be inaccurate due to scattering and wave propagation effects. Hence, they recommended that a careful calibration of this theory is needed before putting it into application. Our numerical simulations and theoretical modelling are both quasi-static and, hence, are not affected by the scattering and propagation phenomena. However, the failure in the theoretical formulas of dry fracture compliance values indicates that we also need to calibrate the linear-slip theory here due to the boundary effects and other possible reasons previously stated.

Hence, we calibrate the linear-slip theory by inverting the dry fracture compliance values from the stiffness matrix of the dry 2D samples $\mathbf{C}^{2D}$, which is provided by the numerical simulations. To do so, we first invert the stiffness matrix $\mathbf{C}^{2D}$, which gives the compliance matrix $\mathbf{S}^{2D}$. Based on the linear-slip theory, the fracture compliance values are then obtained by subtracting the compliance values of the 2D dry background medium from $\mathbf{S}^{2D}$ as follows:

$$Z_{Ni} = S_{ii}^{2D} - 1/E_b^{2D}, i = 1, 2, \tag{15}$$

$$Z_{T1} + Z_{T2} = S_{66}^{2D} - 2\left(1 + v_b^{2D}\right)/E_b^{2D}, \tag{16}$$

where S_{ii}^{2D} is the corresponding component of matrix $\mathbf{S}^{2D}$, and v_b^{2D} is the 2D Poisson's ratio, which is related to the 3D Poisson's ratio as follows:

$$v_b^{2D} = \frac{v_b}{1 - v_b}. \tag{17}$$

This method only allows for the estimation of the sum of the tangential excess compliance values of the two fracture sets. Since the two fracture sets are generated in the same fashion, it is reasonable to assume that they have the same value of Z_N/Z_T. This value will be equal to $(Z_{N1}+Z_{N2})/(Z_{T1}+Z_{T2})$. Hence, we can obtain the following expression for Z_{Ti}:

$$Z_{Ti} = Z_{Ni}\frac{Z_{T1} + Z_{T2}}{Z_{N1} + Z_{N2}}, i = 1, 2. \tag{18}$$

However, it is important to notice here that potential departures from equation (18) are not expected to affect the resulting elastic properties of the 2D samples, as only the sum of Z_{T1} and Z_{T2}, not the individual values, is involved in the final expression of the compliance matrix in the 2D case.

In the following sections, we will use the inverted dry fracture compliance values in calculating the elastic properties of the saturated samples at different frequency regimes.

3.2 Low-frequency limit

In the low-frequency limit, the fluid in the fractures has enough time to communicate with that of the background pores and of other fractures, resulting in uniform fluid pressure throughout the pore and fracture space. Hence, the elastic properties for the saturated sample can be obtained from those for the dry sample by using anisotropic Gassmann equations (Gassmann 1951; Gurevich 2003). The compliance matrix of the dry fractured sample $\mathbf{S}^0$ is first obtained through equation (6) using the inverted dry fracture compliance values (Z_{T3} and Z_{T4} are not needed for 2D samples). Then, the saturated stiffness matrix $\mathbf{C}^{\text{sat\_lf}}$ can be computed from the dry stiffness matrix $\mathbf{C}^0$ (inverse of $\mathbf{S}^0$) as follows:

$$c_{ij}^{sat\_lf} = c_{ij}^0 + \alpha_i^0 \alpha_j^0 M_0, i, j = 1, \ldots, 6, \tag{19}$$

where

$$\alpha_m^0 = 1 - \frac{\sum_{n=1}^3 c_{mn}^0}{3K_g}, \tag{20}$$

for $m = 1, 2$, and 3, $\alpha_4^0 = \alpha_5^0 = \alpha_6^0 = 0$, and the scalar M_0 is the direct analogue of Gassmann's pore space modulus:

$$M_0 = \frac{K_g}{(1 - K_0^*/K_g) - \phi(1 - K_g/K_f)}. \tag{21}$$

In equation (21), K_g and K_f are the grain and fluid bulk moduli, respectively; ϕ is the overall porosity (including the

background and fracture porosity); and K_0^* denotes the generalised drained bulk modulus, which is defined as:

$$K_0^* = \frac{1}{9} \sum_{i=1}^3 \sum_{j=1}^3 c_{ij}^0. \tag{22}$$

This procedure of obtaining $\mathbf{C}^{\text{sat\_lf}}$ is schematically illustrated in Fig. 3.

3.3 Intermediate frequency range

In the intermediate frequency range, due to the low permeability of the background, there is no time for communication between the fluid of such region and that of the fractures, i.e., fractures are hydraulically isolated from the background medium. However, as open fractures are characterised by very high permeability values, there is enough time for the fluid pressure of intersecting fractures to equilibrate at a common value. In these conditions, the isotropic Gassmann equations can be applied first to calculate the elastic properties of the saturated background medium:

$$K_b^{sat} = K_b + \alpha^2 M_b, \tag{23}$$

$$G_b^{sat} = G_b, \tag{24}$$

where K_b^{sat} and G_b^{sat} are the bulk and shear moduli of the saturated background medium, respectively, and α and M_b are the Biot–Willis coefficient and the pore space modulus for the background medium, respectively, which can be expressed as:

$$\alpha = 1 - \frac{K_b}{K_g}, \tag{25}$$

$$M_b = \frac{K_g}{(1 - K_b/K_g) - \phi(1 - K_g/K_f)}. \tag{26}$$

Then, the linear-slip theory is used to obtain the compliance matrix $\mathbf{S}^1$ for the saturated background medium permeated with the dry fractures:

$$\mathbf{S}^1 = \begin{pmatrix} 1/E_b^{sat} + Z_{N1} & -v_b^{sat}/E_b^{sat} & -v_b^{sat}/E_b^{sat} & 0 & 0 & 0 \\ -v_b^{sat}/E_b^{sat} & 1/E_b^{sat} + Z_{N2} & -v_b^{sat}/E_b^{sat} & 0 & 0 & 0 \\ -v_b^{sat}/E_b^{sat} & -v_b^{sat}/E_b^{sat} & 1/E_b^{sat} & 0 & 0 & 0 \\ 0 & 0 & 0 & \frac{2(1+v_b^{sat})}{E_b^{sat}} + Z_{T4} & 0 & 0 \\ 0 & 0 & 0 & 0 & \frac{2(1+v_b^{sat})}{E_b^{sat}} + Z_{T3} & 0 \\ 0 & 0 & 0 & 0 & 0 & \frac{2(1+v_b^{sat})}{E_b^{sat}} + Z_{T1} + Z_{T2} \end{pmatrix}, \tag{27}$$

where Z_{N1}, Z_{N2}, Z_{T1}, Z_{T2}, Z_{T3}, and Z_{T4} are the normal and tangential excess compliance values for the dry fracture, respectively. For the 2D samples, only Z_{N1}, Z_{N2}, Z_{T1}, and Z_{T2} are needed, which are obtained using the inversion method as previously shown. E_b^{sat} and v_b^{sat} are the bulk and Poisson's ratio of the saturated background, which are related to K_b^{sat} and G_b^{sat} as follows:

$$E_b^{sat} = \frac{9K_b^{sat} G_b^{sat}}{3K_b^{sat} + G_b^{sat}}, \tag{28}$$
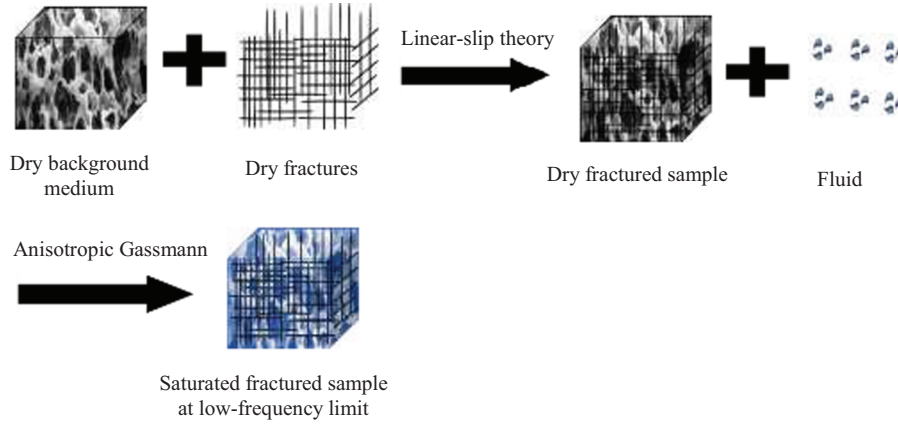
Figure 3 Schematic illustration of the procedure proposed to obtain the stiffness coefficients of the saturated sample at the low-frequency limit.

$$v_b^{sat} = \frac{3K_b^{sat} - 2G_b^{sat}}{2\left(3K_b^{sat} + G_b^{sat}\right)}. \tag{29}$$

Finally, the dry fractures are saturated with fluid by using the anisotropic Gassmann equations, and the stiffness matrix $\mathbf{C}^{sat\_mf}$ of the rock for this frequency range is thus obtained as follows:

$$c_{ij}^{sat\_mf} = c_{ij}^1 + \alpha_i^1 \alpha_j^1 M_1, i, j = 1, \ldots, 6, \tag{30}$$

where c_{ij}^1 is the component of $\mathbf{C}^1$ inversed from $\mathbf{S}^1$; α_m^1 takes the form:

$$\alpha_m^1 = 1 - \frac{\sum_{n=1}^3 c_{mn}^1}{3K_b^{sat}}, \tag{31}$$

and M_1 is expressed as

$$M_1 = \frac{K_b^{sat}}{\left(1 - K_1^*/K_b^{sat}\right) - \phi_f\left(1 - K_b^{sat}/K_f\right)}, \tag{32}$$

where K_1^* is obtained from equation (22) by replacing c_{ij}^0 with c_{ij}^1, and ϕ_f is the volume fraction of the fractures. This procedure for obtaining $\mathbf{C}^{sat\_mf}$ is schematically illustrated in Fig. 4.

It is important to mention that the derivation of the stiffness matrix included here considers that every fracture is intersected by at least another orthogonal fracture, to which its fluid pressure increase can be released. If there are isolated fractures, then the fluid pressure increase in response to the propagation of a seismic wave cannot be relaxed, and therefore, the sample behaves in a stiffer manner. Corresponding modifications could be applied to the model to deal with such situations, but this is beyond the scope of this work.

3.4 High-frequency limit

In the high-frequency limit, the fluid flow not only between background pores and fractures but also between different fractures is negligible. This means that the fluid in each fracture is isolated from both the background medium and the other fractures. The effective fracture compliance is thus decreased due to the fluid effect, and its value can be computed using the theory for isolated fluid-filled fractures (Hudson 1981; Schoenberg and Douma 1988; Gurevich 2003):

$$Z_{Ni}^{sat} = \frac{Z_{Ni}}{1 + \frac{K_f \Delta_{Ni}}{L_b^{sat} \phi_{fi}(1-\Delta_{Ni})}\left(1 - \frac{K_f}{K_b^{sat}}\right)^{-1}}, i = 1, 2, \tag{33}$$

$$Z_{Ti}^{sat} = Z_{Ti}, i = 1, 2, 3, 4, \tag{34}$$

where Z_{Ni} and Z_{Ti} are the normal and tangential excess compliance values for the dry fractures, respectively. For the 2D samples, only Z_{N1}, Z_{N2}, Z_{T1}, and Z_{T2} are needed, which are obtained using the inversion method as previously shown. L_b^{sat} is the saturated P-wave modulus for the background medium, which is computed as follows:

$$L_b^{sat} = K_b^{sat} + 4/3 G_b^{sat}; \rightarrow . \tag{35}$$

ϕ_{fi} and Δ_{Ni} are the volume fraction and the dimensionless weakness of the corresponding fracture set, respectively. Parameter Δ_{Ni} has the following form:

$$\Delta_{Ni} = \frac{L_b^{sat} Z_{Ni}}{1 + L_b^{sat} Z_{Ni}}, i = 1, 2. \tag{36}$$

Hence, the elastic properties of the sample can be calculated by first applying the isotropic Gassmann equations [equations (23) and (24)] to the background medium and then taking into account the influence of these isolated fractures
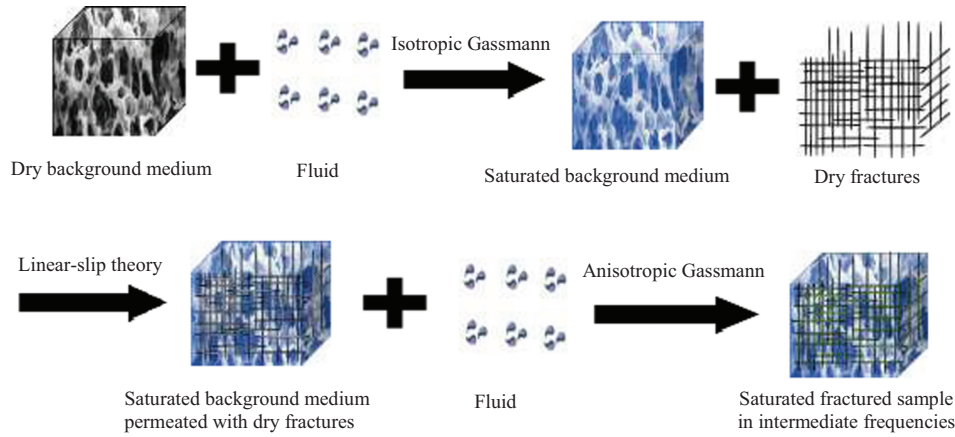
Figure 4 Schematic illustration of the procedure proposed to obtain the stiffness coefficients of the saturated sample in the intermediate frequency range.

with effective compliance values by using the linear-slip theory (Gurevich 2003). The resulting compliance matrix $\mathbf{S}^{sat\_hf}$ is as follows:

$$\mathbf{S}^{sat\_hf} = \begin{pmatrix} 1/E_b^{sat} + Z_{N1}^{sat} & -v_b^{sat}/E_b^{sat} & -v_b^{sat}/E_b^{sat} & 0 & 0 & 0 \\ -v_b^{sat}/E_b^{sat} & 1/E_b^{sat} + Z_{N2}^{sat} & -v_b^{sat}/E_b^{sat} & 0 & 0 & 0 \\ -v_b^{sat}/E_b^{sat} & -v_b^{sat}/E_b^{sat} & 1/E_b^{sat} & 0 & 0 & 0 \\ 0 & 0 & 0 & \frac{2(1+v_b^{sat})}{E_b^{sat}} + Z_{T4}^{sat} & 0 & 0 \\ 0 & 0 & 0 & 0 & \frac{2(1+v_b^{sat})}{E_b^{sat}} + Z_{T3}^{sat} & 0 \\ 0 & 0 & 0 & 0 & 0 & \frac{2(1+v_b^{sat})}{E_b^{sat}} + Z_{T1}^{sat} + Z_{T2}^{sat} \end{pmatrix}. \tag{37}$$

The stiffness matrix $\mathbf{C}^{sat\_hf}$ of the rock in the high-frequency limit can be obtained by taking the inverse of $\mathbf{S}^{sat\_hf}$. This procedure of obtaining $\mathbf{C}^{sat\_hf}$ is schematically illustrated in Fig. 5.

Once the stiffness matrices are computed for the three regimes, the P- and S-wave velocities for any angle of incidence can be obtained by using standard equations for anisotropic media (Mavko, Mukerji, and Dvorkin 2009).

3.5 Characteristic frequencies

Two characteristic frequencies exist for rocks having intersecting fractures. The first characteristic frequency represents the location of the attenuation peak and the largest slope for the dispersion due to the wave-induced fluid flow between the background medium and the fractures (FB-WIFF; Rubino *et al.* 2014). The relevant spatial scale for this FB-WIFF is the diffusion length l (Galvin and Gurevich 2006, 2007):

$$l = \sqrt{\frac{2D_b}{f}}, \tag{38}$$

where f is the frequency of the seismic wave, and D_b is the hydraulic diffusivity of the background medium. This diffusivity has the following form:

$$D_b = \frac{M_b L_b \kappa_b}{\eta L_b^{sat}}, \tag{39}$$

where L_b is the dry P-wave modulus for the background medium as follows:

$$L_b = K_b + 4/3 G_b; \tag{40}$$

κ_b is the permeability of the background medium; η is the fluid viscosity. For a medium with sets of randomly distributed aligned fractures as shown in Fig. 1, maximum attenuation due to FB-WIFF occurs when the diffusion length l is of similar size as the radius of the fractures a_f (Galvin and Gurevich 2006, 2007). Therefore, the characteristic frequency f_{FB} for FB-WIFF has the following form:

$$f_{FB} = \frac{2D_b}{a_f^2}. \tag{41}$$

The second characteristic frequency denotes the location of the attenuation peak and the largest slope for the dispersion due to the wave-induced fluid flow within connected fractures (FF-WIFF; Rubino *et al.* 2014). At this frequency range, typically, the fractures are hydraulically isolated from
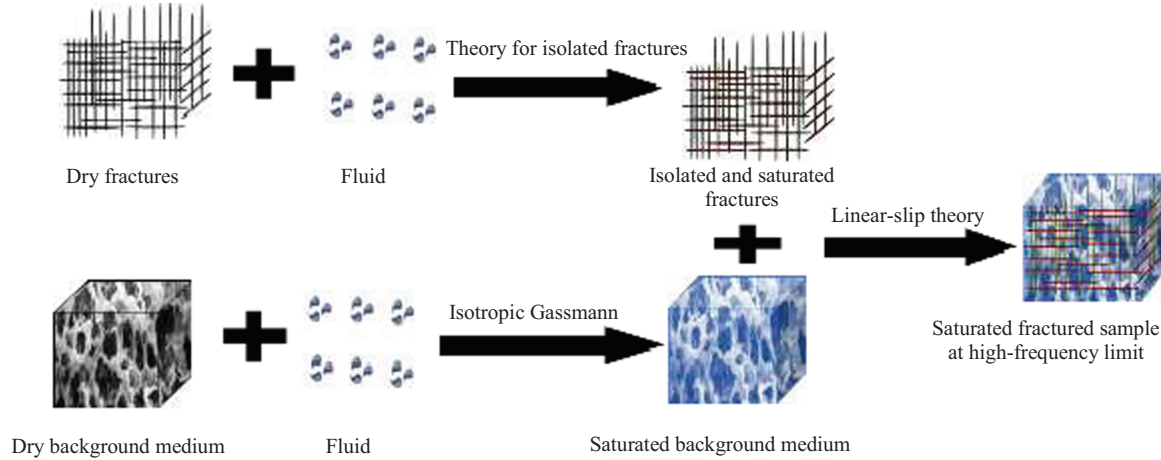
Figure 5 Schematic illustration of the procedure proposed to obtain the stiffness coefficients of the saturated sample at the high-frequency limit.

the background medium. When a fracture set is oriented perpendicular to the P-wave propagation direction, it experiences a fluid pressure increase (or decrease) in response to the stresses applied by the perturbation. The fluid is thus injected into (or withdrawn from) a medium composed of the fracture set parallel to the P-wave propagation direction and the saturated background medium, where the fracture set and the saturated background act as the pore space and the solid (grain) phase, respectively. Similar to the diffusivity of the background medium [equation (39)], the diffusivity D_e for this effective medium should take the following form:

$$D_e = \frac{M_e L_e \kappa_e}{\eta L_e^{sat}}, \tag{42}$$

where M_e is the effective pore space modulus for this medium; L_e and L_e^{sat} are the dry and saturated effective P-wave moduli, respectively, and κ_e is the effective permeability.

In equation (42), the elastic properties of the effective medium are needed to calculate its diffusivity. The dry stiffness matrix $\mathbf{C}^e$ can be obtained using the linear-slip theory. Then, the saturated stiffness matrix $\mathbf{C}^{e\text{-}sat}$ is computed using the anisotropic Gassmann equations. The parameters in equation (42) thus can be calculated as follows:

$$M_e = \frac{K_b^{sat}}{\left(1 - K_e/K_b^{sat}\right) - \phi_e \left(1 - K_b^{sat}/K_f\right)}, \tag{43}$$

$$L_e = \frac{C_{11}^e + C_{22}^e + C_{33}^e}{3}, \tag{44}$$

$$L_e^{sat} = \frac{C_{11}^{e\text{-}sat} + C_{22}^{e\text{-}sat} + C_{33}^{e\text{-}sat}}{3}, \tag{45}$$

where K_b^{sat} is the saturated bulk modulus for the background medium; ϕ_e is the fracture porosity contained in this medium;

C_{ij}^e and $C_{ij}^{e\text{-}sat}$ are the components of the stiffness matrix for the dry and saturated moduli, respectively; K_f is the fluid bulk modulus; and K_e denotes the generalised bulk modulus for this medium, which can be calculated using equation (22) by replacing C_{ij}^0 with C_{ij}^e.

Another important parameter to be determined is the effective permeability κ_e for this medium. Since the fluid only flows in the fractures of this medium, the effective permeability should be that of the fractures times the fraction of the fractures according to the definition of permeability, i.e.,

$$\kappa_e = \kappa_{fr} \phi_e. \tag{46}$$

Energy dissipation due to FF-WIFF occurs primarily in the fractures of this effective medium as, for these frequencies, fluid only flows within connected fractures (Rubino *et al.* 2013, 2014). Maximum attenuation thus occurs when the fluid penetrates into the largest possible depth inside connected fractures or, in other words, when the effective diffusion length l computed using diffusivity D_e is comparable to the radius of fractures a_f (Gurevich *et al.* 2009). The characteristic frequency f_{FF} for FF-WIFF is then given by

$$f_{FF} = \frac{2D_e}{a_f^2}. \tag{47}$$

4 RESULTS AND DISCUSSIONS

Using the dry fracture compliance values obtained from the inversion method, the elastic properties in the low- and high-frequency limits and in the intermediate frequency range are computed based on the theoretical framework proposed in this work. The results for the two synthetic samples depicted in Fig. 1 are shown as solid circles in Fig. 2, together with
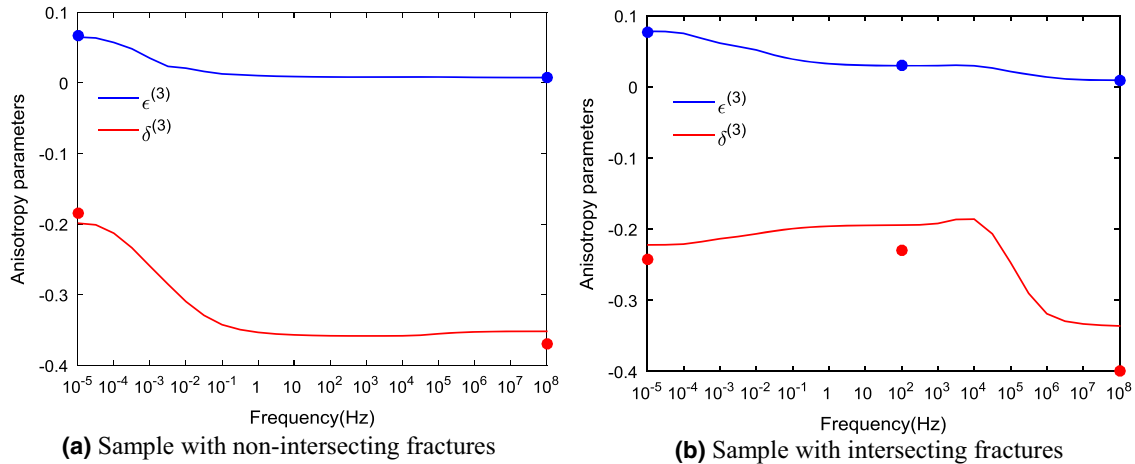
Figure 6 Thomsen-style anisotropy parameters for the two 2D samples computed using the stiffness coefficients obtained from (solid lines) the numerical simulations and (solid circles) the theoretical predictions.

the numerical simulation results. For the sample with non-intersecting fracture sets, there is no communication between the fluids of different fractures for frequencies close to f_{FF}. Therefore, only the low- and high-frequency limits exist in this case. However, an intermediate frequency range arises for the sample with intersecting fractures due to fluid pressure communication between the orthogonal fracture sets.

Comparing the theoretical predictions with the numerical simulations, it is found that they are in good agreement with each other. The maximum discrepancies between the estimations given by the two approaches occur for coefficient C_{66}. There are two possible reasons for the discrepancies. One reason is that the numerical simulations consider generic anisotropy for the resulting equivalent medium, whereas the theoretical methodology approximates the medium as orthotropic. The other reason is the limited volume of the samples in the numerical simulations, which can produce boundary effects on the resulting average properties.

Apart from the elastic properties, the characteristic frequencies for FB-WIFF and FF-WIFF are also computed and shown in Fig. 2 (vertical solid lines). We observe that the estimated characteristic frequencies are in very good agreement with the numerical simulations as they fall in the transition regimes of the stiffness coefficients. Equations (41) and (47) suggest that, while the characteristic frequency for FF-WIFF is directly proportional to fracture permeability, the fracture permeability has no influence on the FB-WIFF characteristic frequency. To verify this, we double the fracture permeability for the sample with intersecting fractures while keeping the other parameters constant and repeat the numerical

simulations. The dashed lines in Fig. 2 show that, indeed, the transition regime for FB-WIFF is not influenced, but that for FF-WIFF shifts towards higher frequencies. This result is consistent with our proposed formulas and thus supports their applicability. In this context, it is important to mention that, while Rubino *et al.* (2014) verified that the location in the frequency axis of the attenuation peak related to FF-WIFF due to the propagation of a P-wave in the vertical direction of wave propagation is directly proportional to the permeability of the fracture material, the corresponding analysis for the components of the stiffness matrix of the effective medium was missing. The verification of the dependence of the FF-WIFF transition frequency on the mechanical properties of the background and fracture material and on the fracture length proposed in this paper will be the subject of future work.

Furthermore, since the dry samples are characterised by anelliptical anisotropy, it is interesting to explore how the theory accurately predicts the anisotropy parameters of the saturated samples at different frequencies. To do so, we compute anisotropy parameters $\delta^{(3)}$ and $\varepsilon^{(3)}$ using both the results of the numerical simulations and those obtained from the theoretical framework. Figure 6 shows that there is very good agreement between the anisotropy parameters provided by the two approaches. The largest discrepancies occur for parameter $\delta^{(3)}$ in the case of the sample with intersecting fractures and in the high-frequency limit. This is primarily caused by the discrepancies between the values of C_{12} and C_{66} obtained from the numerical simulations and from the theoretical predictions.

5 CONCLUSIONS

In this work, we have developed a theoretical framework to quantify the effects of intersecting fractures on the frequency-dependent elastic properties of saturated porous rocks. The dry fracture compliance values were computed using an inversion method. Then, the effective stiffness coefficients of the saturated samples were obtained in the low- and high-frequency limits and for an intermediate frequency range for which there is no fluid communication between fractures and the background while fluid pressure within intersecting fractures is at equilibrium. In addition, the characteristic frequencies for FB-WIFF and FF-WIFF, which separate the three frequency regimes, were rigorously determined. We observed very good agreement between the theoretical predictions of stiffness coefficients, Thomsen-style anisotropic parameters, and characteristic frequencies and the values obtained from corresponding numerical simulations. The proposed theoretical framework is easy to apply, is applicable not only to 2D but also to 3D fracture systems, and could thus be employed in inversion schemes designed to characterise fractured environments.

REFERENCES

Biot M.A. 1941. General theory of three-dimensional consolidation. *Journal of Applied Physics* **12**, 155–164.

Biot M.A. 1962. Mechanics of deformation and acoustic propagation in porous media. *Journal of Applied Physics* **33**, 1482–1498.

Chapman M., Zatsepin S.V. and Crampin S. 2002. Derivation of a microstructural poroelastic model. *Geophysical Journal International* **151**, 427–451.

Chapman M. 2003. Frequency-dependent anisotropy due to meso-scale fractures in the presence of equant porosity. *Geophysical Prospecting* **51**, 369–379.

Collet O., Gurevich B., Madadi M. and Pervukhina M. 2014. Modeling elastic anisotropy resulting from the application of triaxial stress. *Geophysics* **79**(5), C135–C145.

Dutta N.C. and Odé H. 1979. Attenuation and dispersion of compressional waves in fluid-filled porous rocks with partial gas saturation (White model)—Part I: Biot theory. *Geophysics* **44**(11), 1777–1788.

Endres A.L. and Knight R.J. 1997. Incorporating pore geometry and fluid pressure communication into modeling the elastic behavior of porous rocks. *Geophysics* **62**(1), 106–117.

Far M.E., Thomsen L. and Sayers C.M. 2013. Seismic characterization of reservoirs with asymmetric fractures. *Geophysics* **78**(2), N1–N10.

Galvin R.J. and Gurevich B. 2006. Interaction of an elastic wave with a circular crack in a fluid-saturated porous medium. *Applied Physics Letters* **88**, 061918.

Galvin R.J. and Gurevich B. 2007. Scattering of a longitudinal wave by a circular crack in a fluid-saturated porous medium. *International Journal of Solids and Structures* **44**, 7389–7398.

Gassmann F. 1951. Elastic waves through a packing of spheres. *Geophysics* **16**(4), 673–685.

Grechka V. and Kachanov M. 2006. Effective elasticity of rocks with closely spaced and intersecting cracks. *Geophysics* **71**, D85–D91.

Grenon M. and Hadjigeorgiou J. 2012. Application of fracture system models (FSM) in mining and civil rock engineering design. *International Journal of Mining, Reclamation and Environment* **26**(1), 55–73.

Guéguen Y. and Sarout J. 2009. Crack-induced anisotropy in crustal rocks: predicted dry and fluid-saturated Thomsen's parameters. *Physics of the Earth and Planetary Interiors* **172**, 116–124.

Gurevich B. 2003. Elastic properties of saturated porous rocks with aligned fractures. *Journal of Applied Geophysics* **54**, 203–218.

Gurevich B., Brajanovski M., Galvin R.J., Müller T.M. and Toms-Stewart J. 2009. P-wave dispersion and attenuation in fractured and porous reservoirs—poroelasticity approach. *Geophysical Prospecting* **57**, 225–237.

Hudson J.A. 1981. Wave speeds and attenuation of elastic waves in material containing cracks. *Geophysical Journal of the Royal Astronomical Society* **64**, 133–150.

Jakobsen M. 2004. The interacting inclusion model of wave-induced fluid flow. *Geophysical Journal International* **158**, 1168–1176.

Jones T.D. 1986. Pore fluids and frequency-dependent wave propagation in rocks. *Geophysics* **51**(10), 1939–1953.

Kachanov M. and Sevostianov I. 2005. On quantitative characterization of microstructures and effective properties. *International Journal of Solids and Structures* **42**, 309–336.

Karay G. and Hajnal G. 2015. Modelling of groundwater flow in fractured rocks. *Procedia Environmental Sciences* **25**, 142–149.

Lisjak A., Figi D. and Grasselli G. 2014. Fracture development around deep underground excavations: insights from FDEM modelling. *Journal of Rock Mechanics and Geotechnical Engineering* **6**(6), 493–505.

Luo Z. and Bryant S. 2014. Impacts of injection induced fractures propagation in CO2 geological sequestration—Is fracturing good or bad for CO2 sequestration? *Energy Procedia* **63**, 5394–5407.

Mavko G., Mukerji T. and Dvorkin J. 2009. *The Rock Physics Handbook: Tools for Seismic Analysis of Porous Media*. Cambridge University Press. ISBN: 978-0-521-86136-6.

Nakagawa S. and Schoenberg M.A. 2007. Poroelastic modeling of seismic boundary conditions across a fracture. *The Journal of the Acoustical Society of America* **122**, 831–847.

Neuzil C.E. 2013. Can shale safely host U.S. nuclear waste? *EOS, Transactions, American Geophysical Union* **94**(30), 261–268.

O'Connell R.J. and Budiansky B. 1977. Viscoelastic properties of fluid-saturated cracked solids. *Journal of Geophysical Research* **82**(36), 5719–5735.

Rubino J.G., Guarracino L., Müller T.M. and Holliger K. 2013. Do seismic waves sense fracture connectivity? *Geophysical Research Letters* **40**, 692–696.

Rubino J.G., Müller T.M., Guarracino L., Milani M. and Holliger K. 2014. Seismoacoustic signatures of fractures connectivity. *Journal of Geophysical Research: Solid Earth* **119**, 2252–2271.

Rubino J.G., Caspari E., Milani M., Müller T.M. and Holliger K. 2015. Seismic anisotropy in fractured low-permeability formations: the effects of hydraulic connectivity. 85th SEG annual international meeting, New Orleans, USA, Expanded Abstracts, 3219–3223.

Rubino J.G., Caspari E., Müller T.M., Milani M., Barbosa N.D. and Holliger K. 2016. Numerical upscaling in 2D heterogeneous poroelastic rocks: Anisotropic attenuation and dispersion of seismic waves. *Journal of Geophysical Research: Solid Earth* **121**, 6698–6721.

Sarout J. 2012. Impact of pore space topology on permeability, cut-off frequencies and validity of wave propagation theories. *Geophysical Journal International* **189**, 481–492.

Schoenberg M. and Douma J. 1988. Elastic-wave propagation in media with parallel fractures and aligned cracks. *Geophysical Prospecting* **36**, 571–590.

Schoenberg M. and Sayers C.M. 1995. Seismic anisotropy of fractured rock. *Geophysics* **60**(1), 204–211.

Tsvankin I. 1997. Anisotropic parameters and P-wave velocity for orthorhombic media. *Geophysics* **62**(4), 1292–1309.

Vinci C., Renner J. and Steeb H. 2014. On attenuation of seismic waves associated with flow in fractures. *Geophysical Research Letters* **41**, 7515–7523.

Witherspoon P.A., Wang J.S.Y., Iwai K. and Gale J.E. 1980. Validity of cubic law for fluid flow in a deformable rock fracture. *Water Resources Research* **16**(6), 1016–1024.

Yousef B.M. and Angus D.A. 2016. When do fractured media become seismically anisotropic? Some implications on quantifying fracture properties. *Earth and Planetary Science Letters* **444**, 150–159.